

**Biphase coupled cathode enables all-organic rocking-chair lithium
ion batteries based on crystalline AB-stacked covalent triazine-based
frameworks**

Xiaorong Yan¹, Guoqing Zhao¹, Chuanguang Wu¹, Yujie Dai², Jiakui Xiong², Xinyu Wang², Haiping Yu², Zihui Wang¹, Rui Li², Jingru Liu², Mingjun Hu^{1,*}, Jun Yang^{2,3,*}

*

1 School of Materials Science and Engineering, Beihang University, Beijing 100191, China

2 Beijing Institute of Nanoenergy & Nanosystems, Chinese Academy of Sciences, Beijing 101400, China

3. ShenSi Lab, Shenzhen Institute for Advanced Study, University of Electronic Science and Technology of China, Shenzhen 518110, China

*Corresponding authors.

E-mail: mingjunhu@buaa.edu.cn; yangjun@binn.cas.cn.

Experimental Section

Materials:

1,4-dicyanobenzene (DCB) was purchased from Shanghai Haohong Biomedical Technology Co., Ltd. AlCl₃, KCl, NaCl and Li₃PO₄ were purchased from Shanghai Maclean Biochemical Technology Co., Ltd. Methanol, acetone, dichloromethane, and tetrahydrofuran were purchased from Anhui Zesheng Technology Co., Ltd.

Synthesis of CTF(AB):

The eutectic salt consists of a molar ratio of AlCl₃:NaCl:KCl (61:26:13). Typically, 2 equivalents of 1,4-dicyanobenzene and 1 equivalent of eutectic salts are ground in a mortar and subsequently transferred to a quartz tube. The quartz tube is evacuated ($< 2 \times 10^{-2}$ mbar), flame-sealed, and heated to 200 °C in an oven for 24 h. The quartz tube was opened after cooling down to room temperature and the crude product was stirred in 1 M HCl for 24 h to remove the eutectic salt. Finally, after washing with methanol, acetone, dichloromethane, and tetrahydrofuran to remove the oligomers and drying in a vacuum oven at 80 °C, the CTF sample was obtained.

Synthesis of CTF-M:

Work-up according to the synthesis of CTF but extracted by ball milling in 1 M HCl for 5 h.

Synthesis of CTF-550:

The synthesis CTF was transferred into a crucible with a cover. The crucible was placed in a horizontal tube furnace and heated under atmospheric argon pressure at the ramp rate of 10 °C min⁻¹ to 550 °C for 2 h. CTF-550 was obtained after cooling down to room temperature.

Synthesis of CTF-AA:

Typically, 1 equivalent of 1,4-dicyanobenzene and 1 equivalent of ZnCl₂ are ground in a mortar and subsequently transferred to a quartz tube. The quartz tube is

evacuated ($< 2 \times 10^{-2}$ mbar), flame-sealed, and heated to 400 °C in an oven for 48 h. The quartz tube was opened after cooling down to room temperature and the crude product was stirred in 1 M HCl for 24 h to remove the eutectic salt. Finally, after washing with methanol, acetone, dichloromethane, and tetrahydrofuran to remove the oligomers and drying in a vacuum oven at 80 °C, the CTF sample was obtained.

Electrochemical measurements:

The working electrodes of CTF, CTF-M and CTF-550 were made by mixing the active material with ketjen black and polyvinylidene fluoride (PVDF) binder in NMP (1-methyl-2-pyrrolidone) solution at a weight ratio of 6:3:1. The acquired slurry was coated on Al foil (as the cathode) or Cu foil (as the anode) and dried in a vacuum oven at 80 °C overnight. Lithium metal foil (15.6 mm diameter) was used as the counter electrode and a polypropylene membrane was used as the separator. 1 M lithium hexafluorophosphate (LiPF_6) in ethylene carbonate/diethyl carbonate (EC/DEC) (1:1, v/v) was used as an electrolyte.

The cathode of RCBs was made by mixing CTF-M with Li_3PO_4 , ketjen black and PVDF in NMP solution and then coated on Al foil. The weight ratio CTF-M : Li_3PO_4 was 3:1. The anode of RCB was made by mixing CTF-550 with ketjen black and PVDF in NMP solution at a weight ratio of 6:3:1, and then coated on Al foil. There were no other differences in the battery assembly steps.

Characterizations:

The scanning-electron-microscopy images and energy-dispersive spectroscopy were performed on a Field Emission Scanning Electron Microscopy (Nova Nano SEM-450). The transmission electron microscopy (TEM) images were performed on JEOL JEM-F200 transmission electron microscopy. The atomic force microscopy (AFM) images were performed on Bruker Dimension Icon atomic force microscopy. The ex-situ XRD measurements were carried out on Xpert3 Powder (Cu $K\alpha$ radiation). FTIR spectra were collected on an FTIR spectrophotometer (VERTEX80v, Bruker). XPS measurements were performed on an X-ray photoelectron spectrometer (Thermo

Scientific K-Alpha) using the Al K α monochromatic beam (1486.6 eV), and every spectrum was corrected according to C 1s at 284.8 eV (graphite-like carbon). Elemental analysis (EA) was performed on an elemental analyzer (Elementar UNICUBE). N₂ physisorption measurements were performed on QuantaChrome autosorb iQ2 apparatus at 77 K. The BET method and density functional theory pore model were utilized to calculate the specific surface area and pore size distribution, respectively. TG-IR was performed on TG209F3 and TENSOR. CHI760E electrochemical workstation was used to collect CV curves at different scan rates and Nyquist plots with an amplitude of 5 mV in the frequency range from 0.01 Hz to 100 kHz. The galvanostatic charge and discharge measurements of the assembled cells were performed on a LANHE battery testing system (CT3001A) at 25 °C.

Computational method:

The ground state geometry was optimized using DFT calculations. All calculations are performed with Gaussian 09 package¹ using the B3LYP/6-31G(d) basis sets^{2,3}. Based on the optimized molecular structures the HOMO/LUMO and electrostatic potential (ESP) analysis were visualized with Gauss view 6.0.

Table S1. Comparison of the synthesis methods of CTF.

	Temperature/°C	Solvent	Catalyst	Time/h	Ref.
1	Room temperature	CHCl ₃	CF ₃ SO ₃ H	overnight	4
2	180	DMSO	Cs ₂ CO ₃	36	5
3	160	DMSO	NaHCO ₃	48	6
4	100	CF ₃ SO ₃ H		1.5	7
5	400	ZnCl ₂		40	8
6	200	NaCl-KCl-ZnCl ₂		24	9
7	300	LiTFSI		48	10
8	350	P ₂ O ₅		24	11
9	400	H ₆ P ₄ O ₁₃		24	12
10	180	AlCl ₃ -NaCl-KCl		24	This work

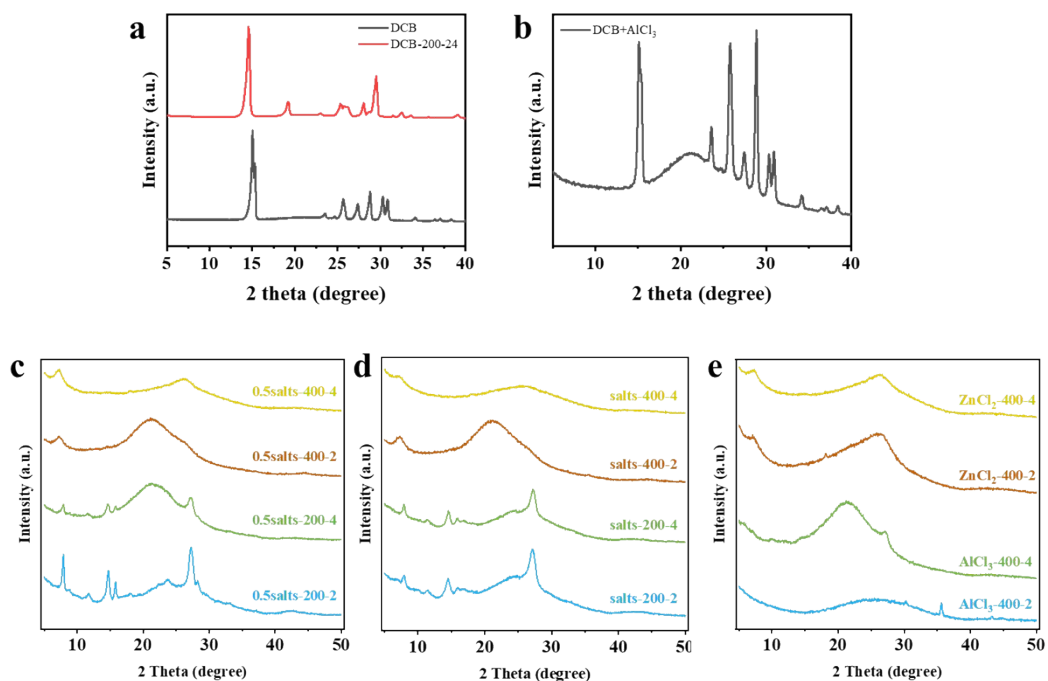


Figure S1. The XRD patterns of (a) pure DCB and DCB heated at 200 °C for 24 h, (b) DCB in pure AlCl₃ heated at 200 °C for 24 h, (c, d) the reaction products of DCB in NaCl-KCl-AlCl₃ molten salt with the ratio of DCB to molten salt (c) 0.5 and (d) 1 after reaction at 200/400 °C for 2/4 days, (e) the reaction products of DCB in ZnCl₂/AlCl₃ molten salt with the ratio of DCB and molten salt 1 after reaction at 400 °C for 2/4 days.

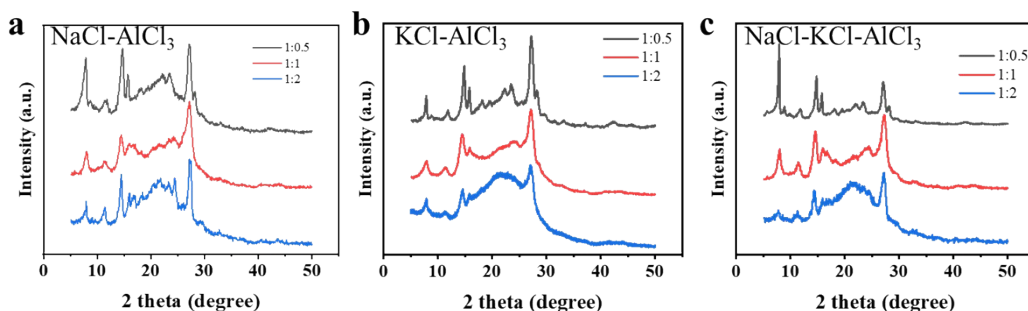


Figure S2 The XRD patterns of the reaction products of DCB in different molten salts and at different ratios of DCB to molten salt after reaction at 200 °C for 24 h, (a) NaCl-AlCl₃, (b) KCl-AlCl₃, (c) NaCl-KCl-AlCl₃.

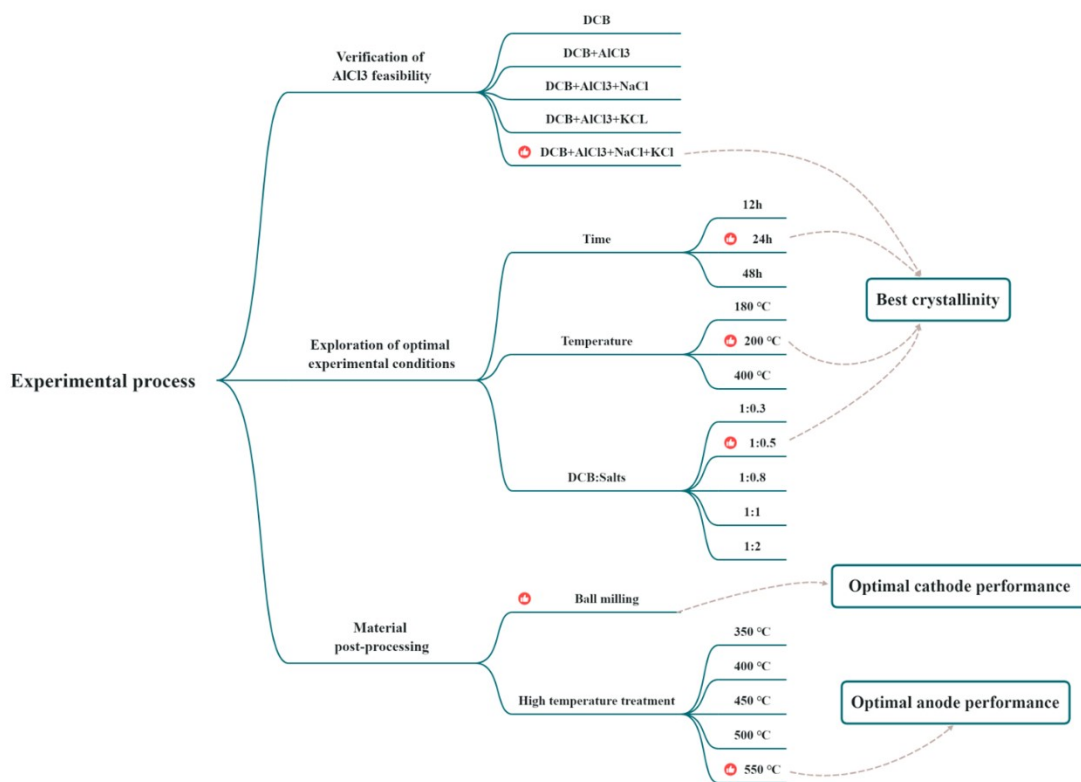


Figure S3. Diagram of the process of exploring optimal synthesis conditions.

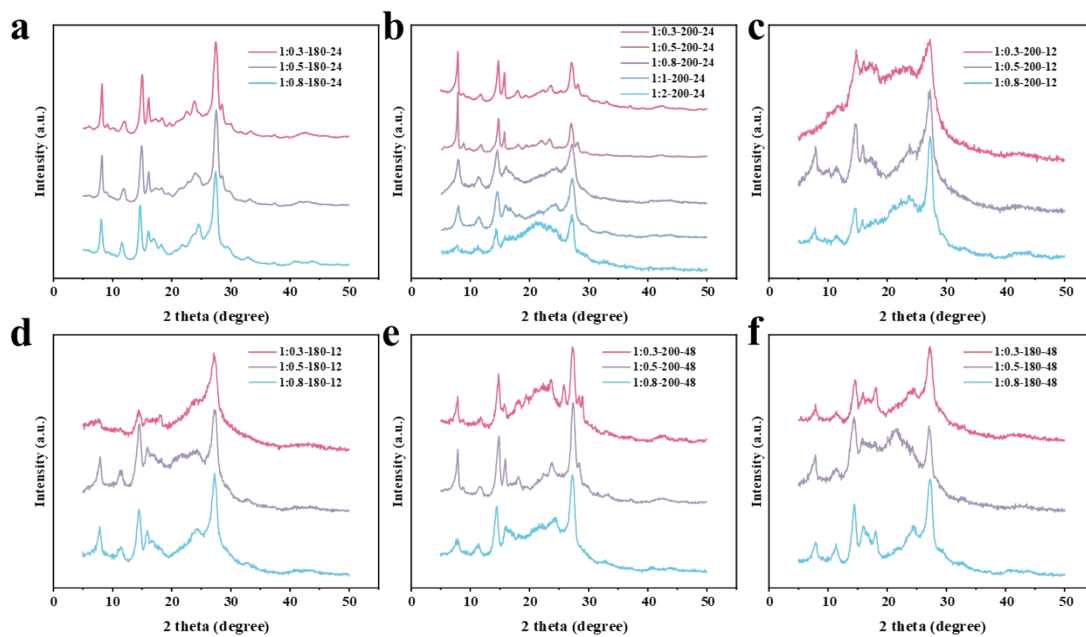


Figure S4. The XRD patterns of the products after reaction at different ratios of DCB to molten salt. (a) at 180 °C for 24 h. (a) at 200 °C for 24 h. (a) at 200 °C for 12 h. (a) at 180 °C for 12 h. (a) at 200 °C for 48 h. (a) at 180 °C for 48 h.

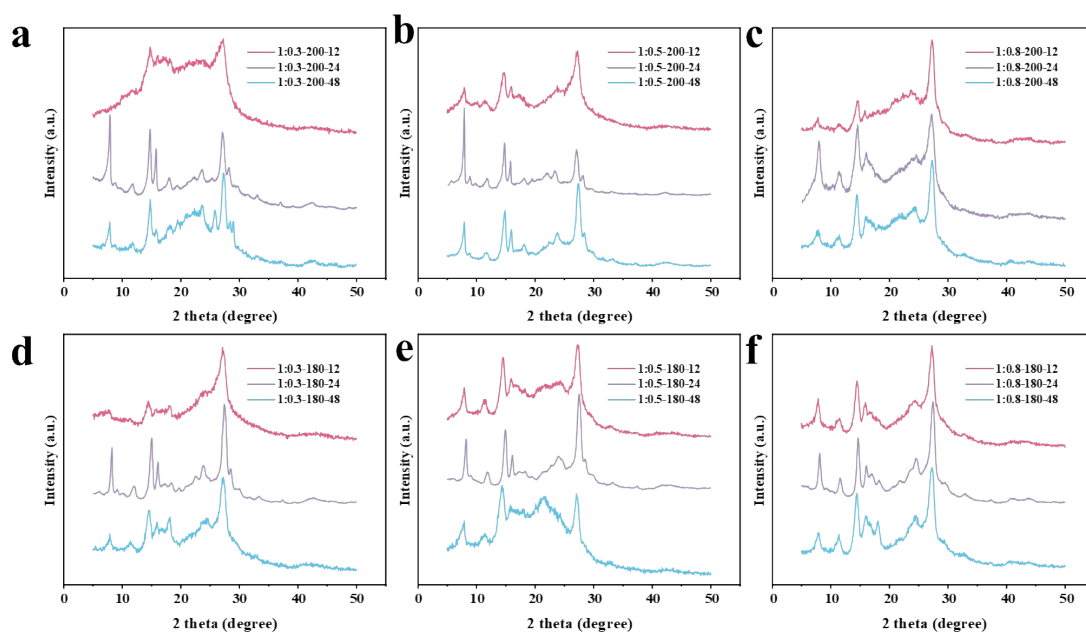


Figure S5. The XRD patterns of the products after reaction at different times. The ratio of DCB to molten salt is (a, d) 1:0.3, (b, e) 1:0.5, (c, f) 1:0.8 and the reaction temperature is (a, b, c) 200 °C, (d, e, f) 180 °C.

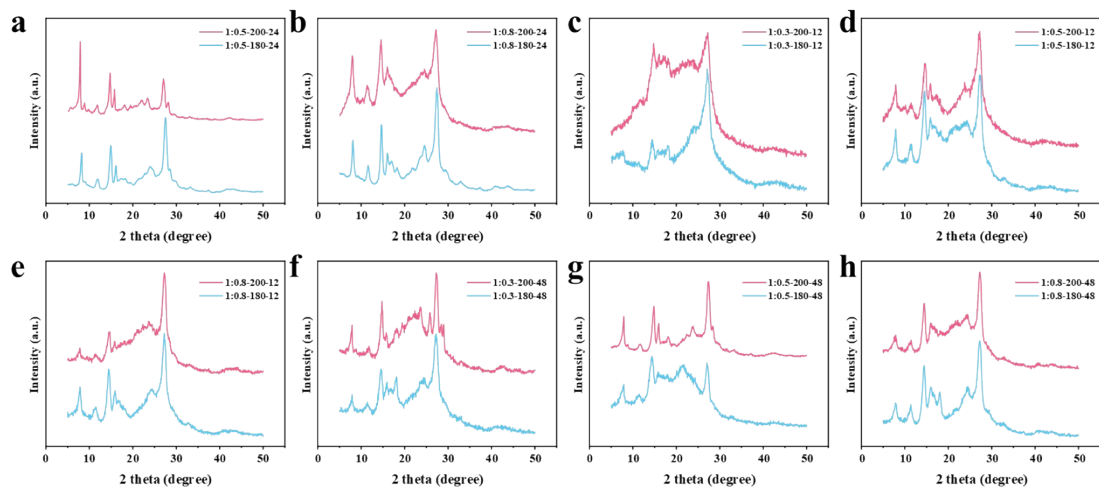


Figure S6. The XRD patterns of the products after reaction at different temperatures. The ratio of DCB to molten salt is (a, d, g) 1:0.5, (b, e, h) 1:0.8, (c, f) 1:0.3 and the reaction time is (a, b) 24 h, (c, d, e) 12 h, (f, g, h) 48 h.

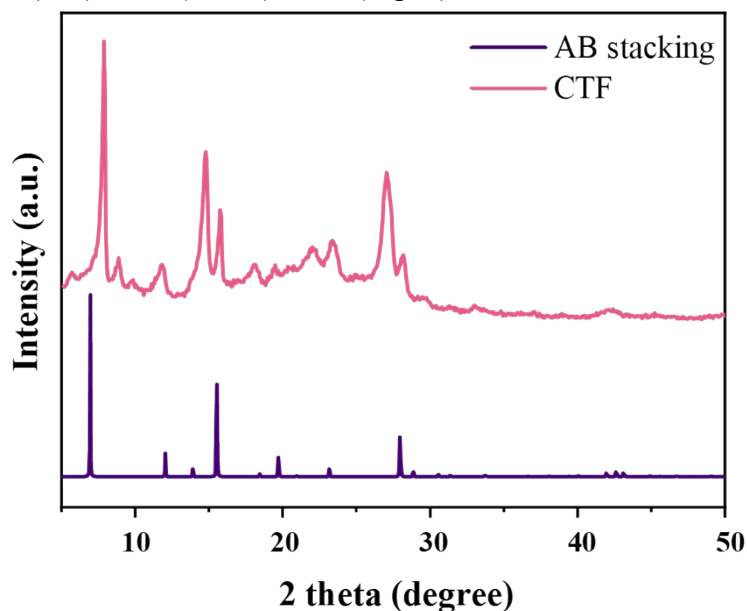


Figure S7. The experimental XRD pattern of CTF and simulated XRD patterns of CTF-1 with AB stacking structures.

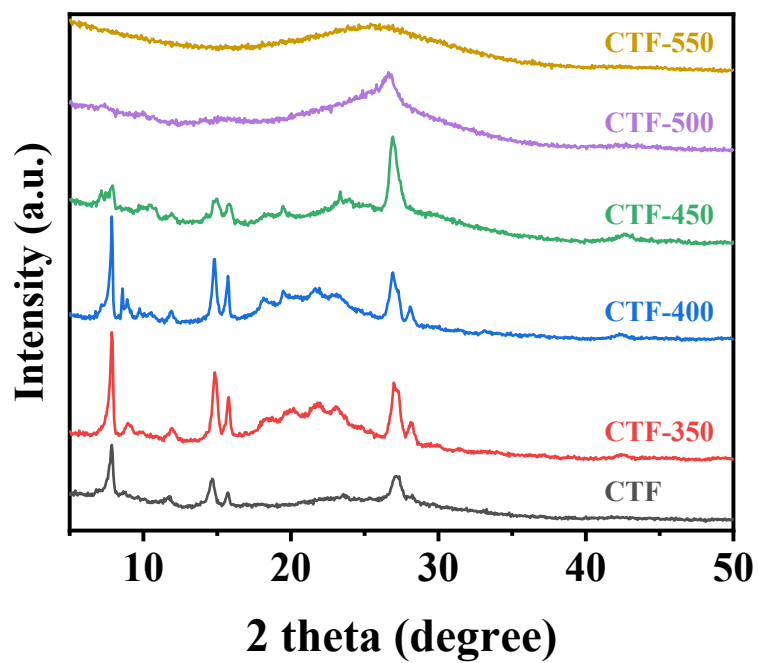


Figure S8. The XRD patterns of CTF after heat treatment at different temperatures.

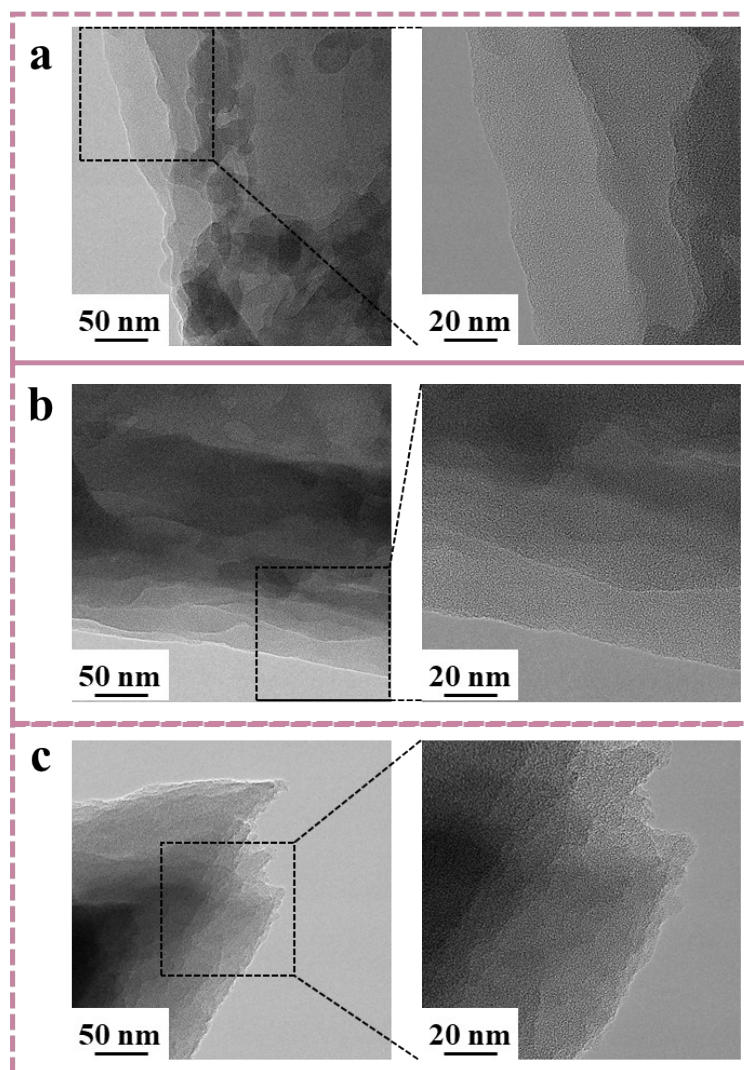


Figure S9. TEM images of (a) CTF, (b) CTF-M and (c) CTF-550.

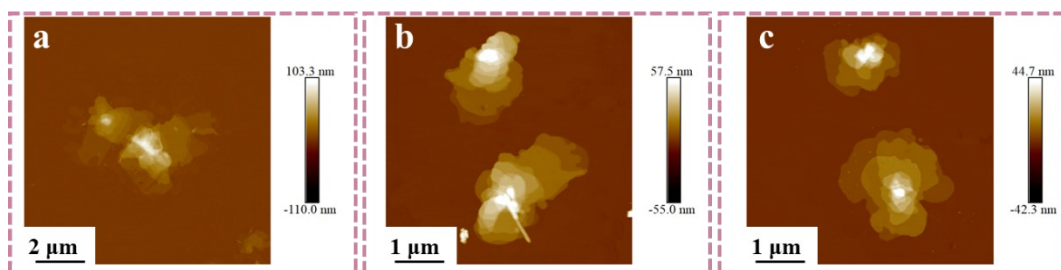


Figure S10. AFM images of (a) CTF, (b) CTF-M and (c) CTF-550.

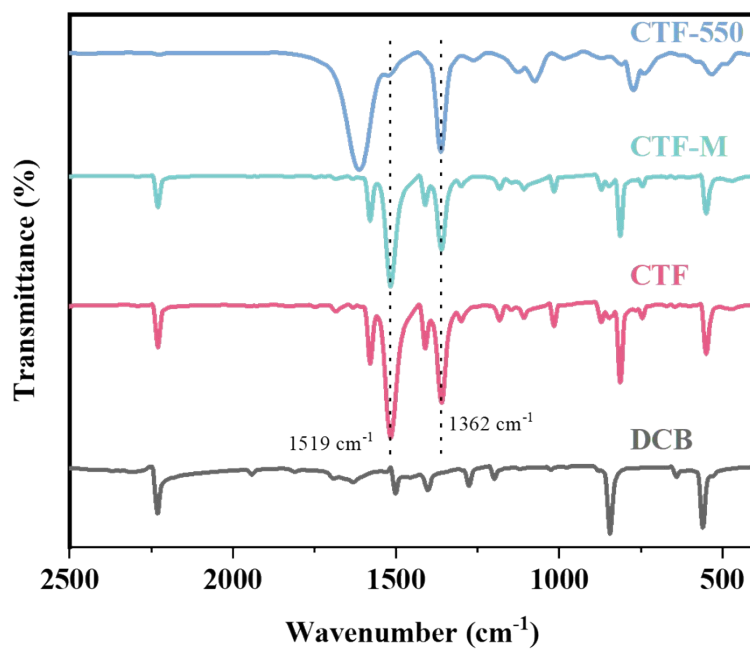


Figure S11. FT-IR spectra of DCB, CTF, CTF-M and CTF-550.

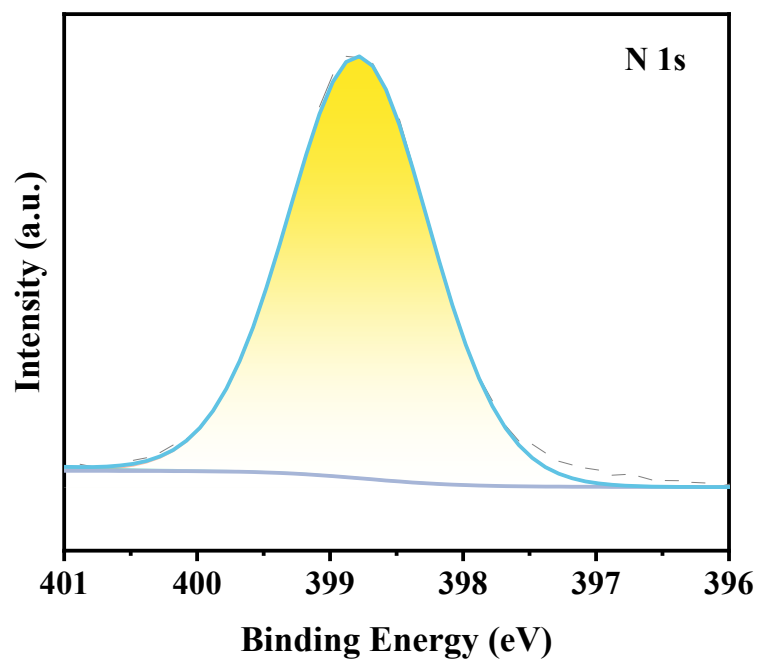


Figure S12. The N 1s XPS spectra of CTF.

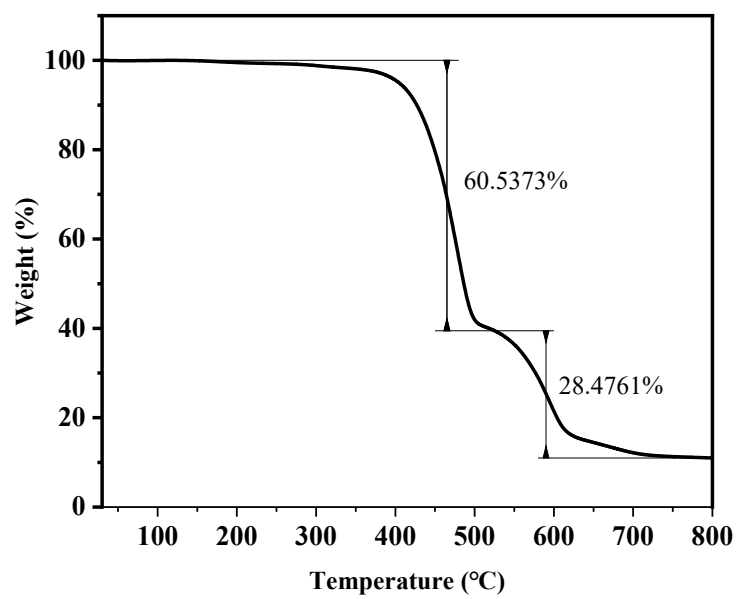


Figure S13. The TGA curves of CTF in N₂.

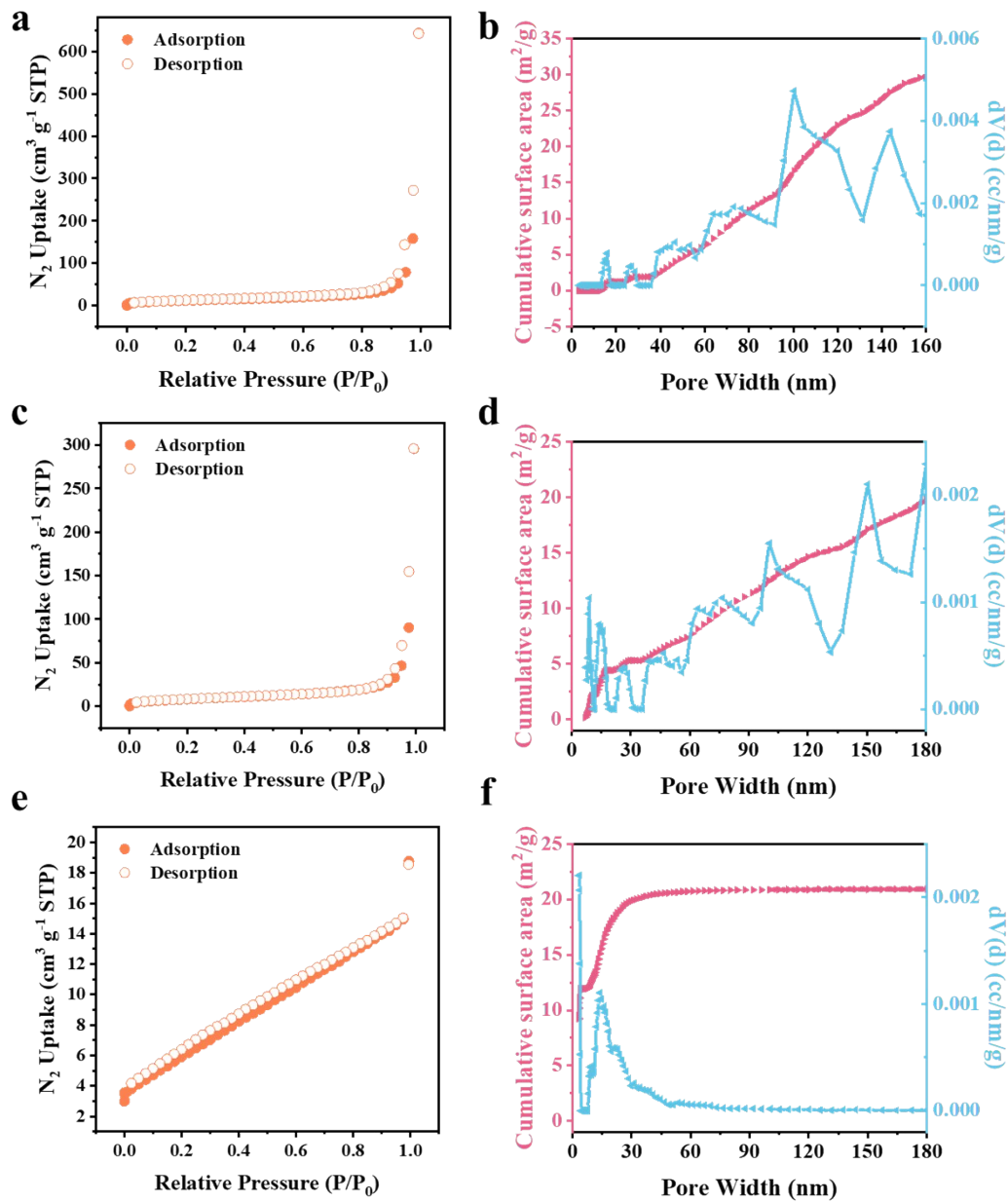


Figure S14. Nitrogen adsorption/desorption isotherms of (a) CTF, (c) CTF-M, (e) CTF-550. Pore size distributions and cumulative density functional theory surface areas of (b) CTF, (d) CTF-M, (f) CTF-550 with pore width.

Table S2. Elemental analysis results of CTF, CTF-M and CTF-550.

Sample	N (wt%)	C (wt%)	H (wt%)	C/N ratio	C/N mole ratio
CTF	20	71.26	2.953	3.563	4.157
CTF-M	19.98	71.25	2.745	3.566	4.160
CTF-550	18.74	70.45	2.207	3.759	4.386

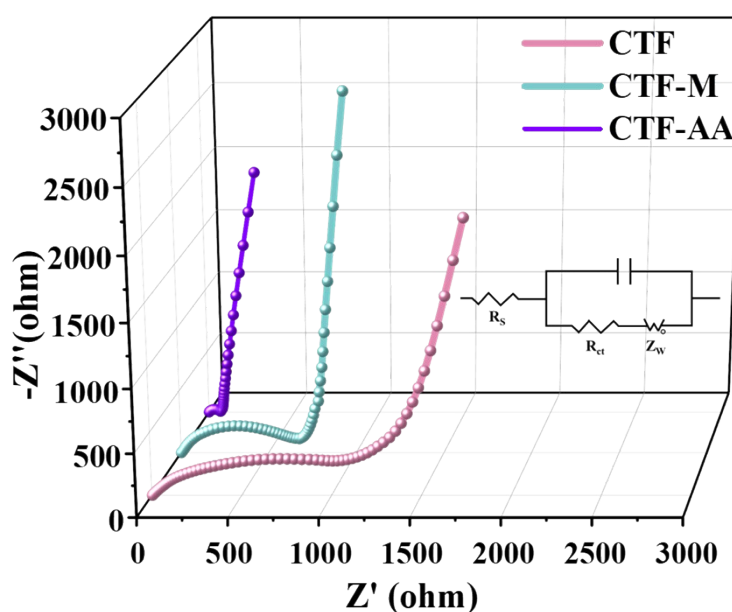


Figure S15. Nyquist plots of CTF, CTF-M, and CTF-AA.

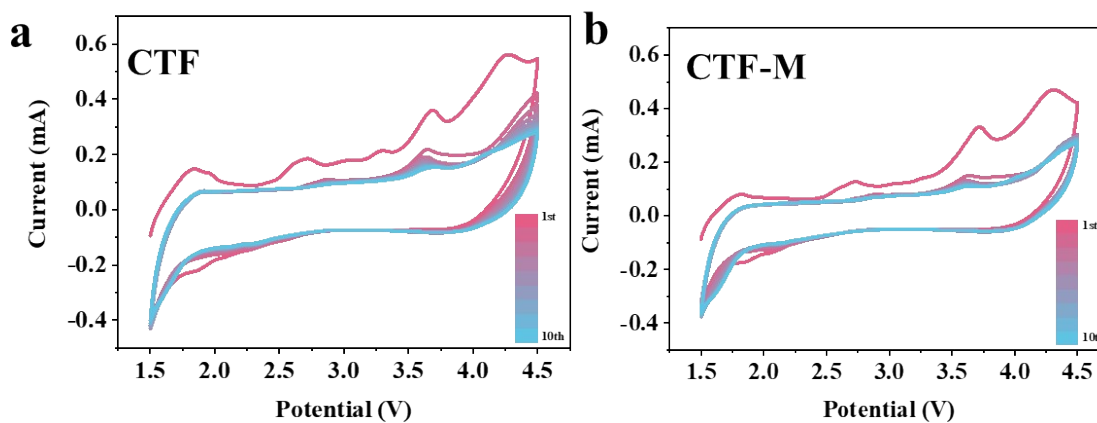


Figure S16. CV curves of (a) CTF, (b) CTF-M at 5 mV s⁻¹.

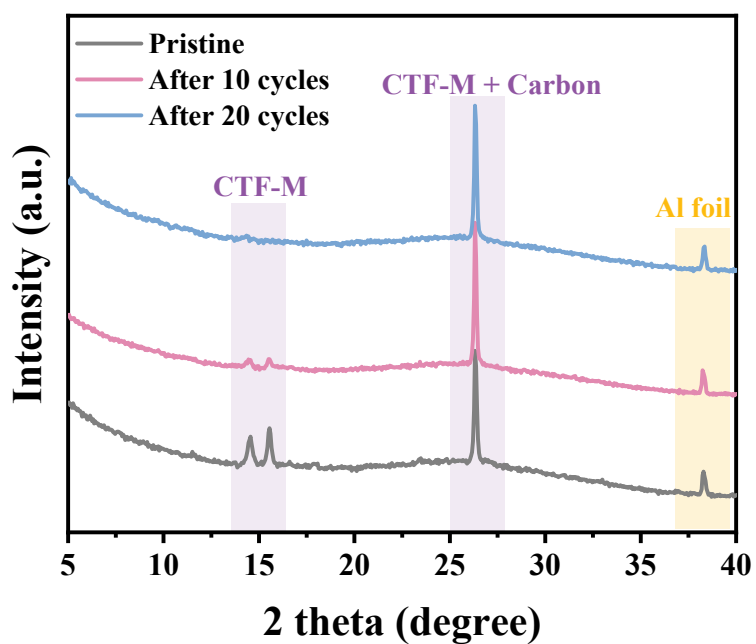


Figure S17. XRD spectra of CTF-M cathode after different cycles.

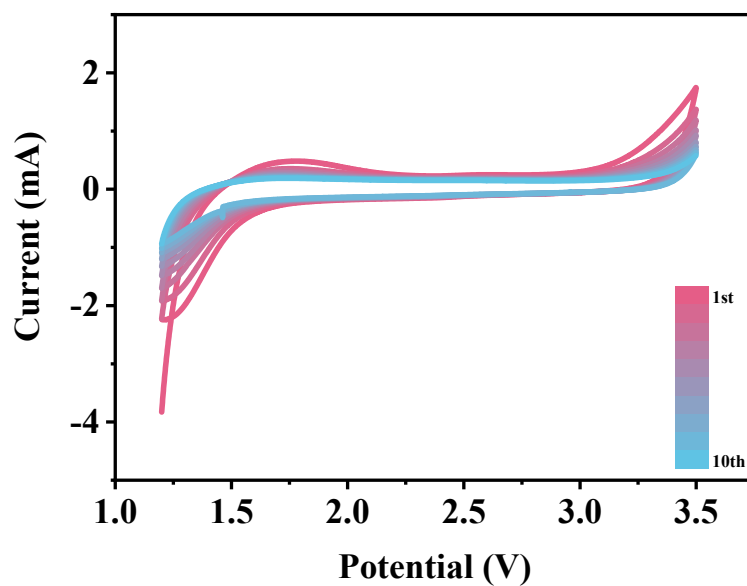


Figure S18. CV curves of CTF-AA at 5 mV s⁻¹.

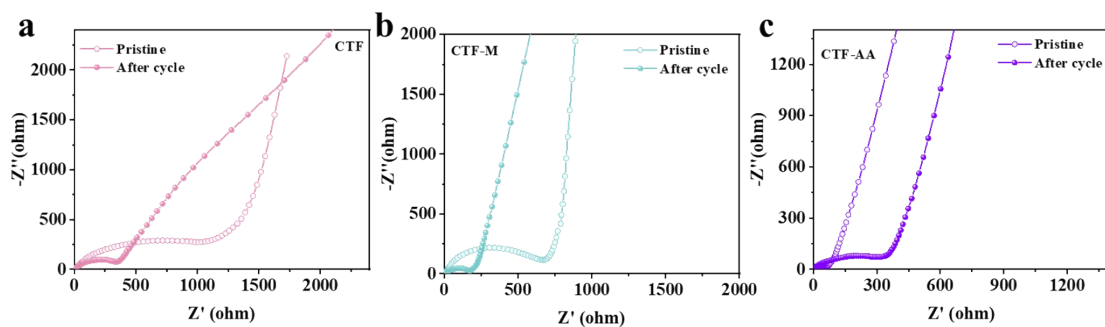


Figure S19. EIS of CTF, CTF-M, and CTF-AA before and after 1000 cycles.

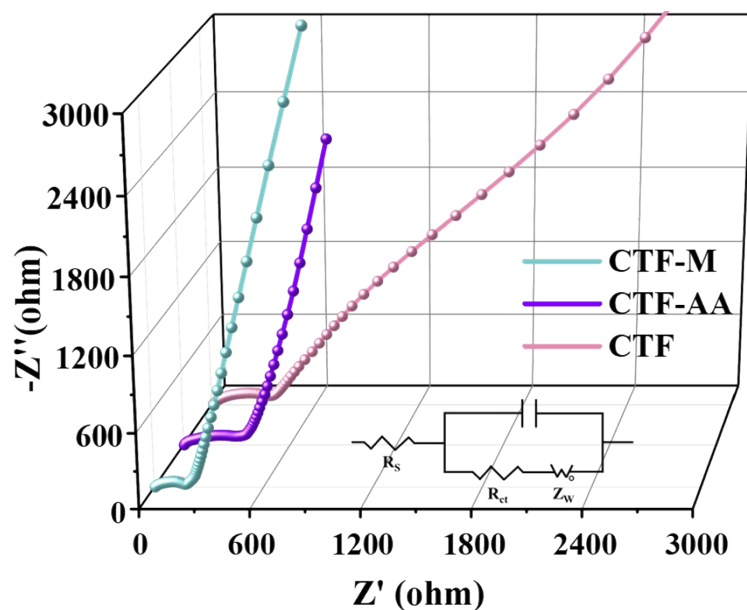


Figure S20. EIS of CTF, CTF-M, and CTF-AA after 1000 cycles.

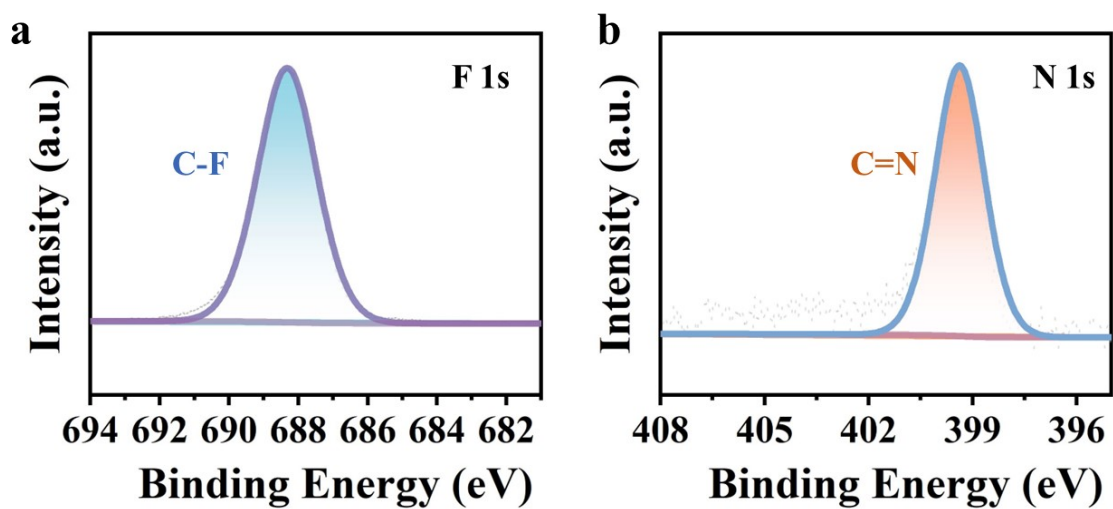


Figure S21. The F 1s and N 1s spectra of the CTF pristine electrode.

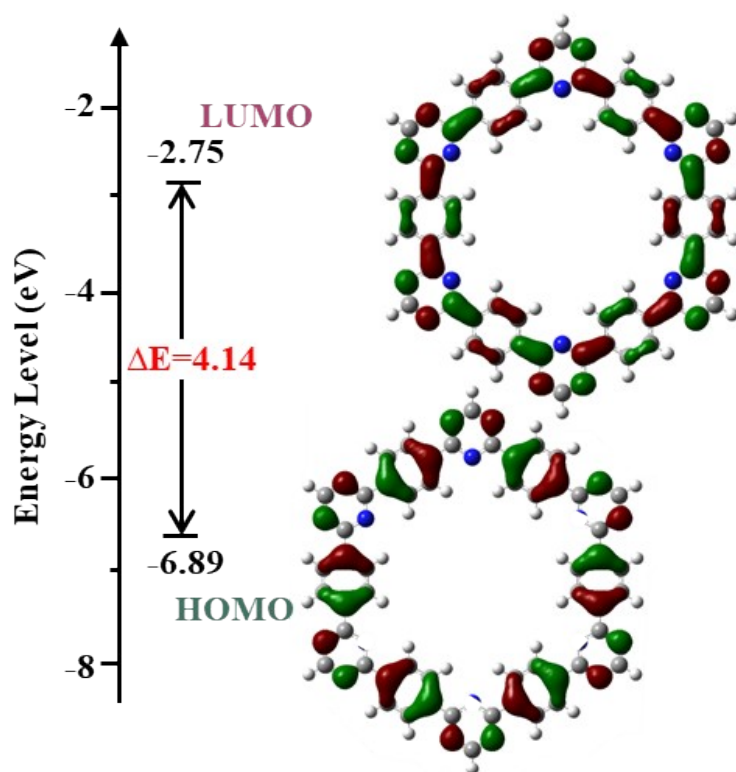


Figure S22. LUMO energy level, HOMO energy level, and HOMO-LUMO energy gap (ΔE) of CTF.

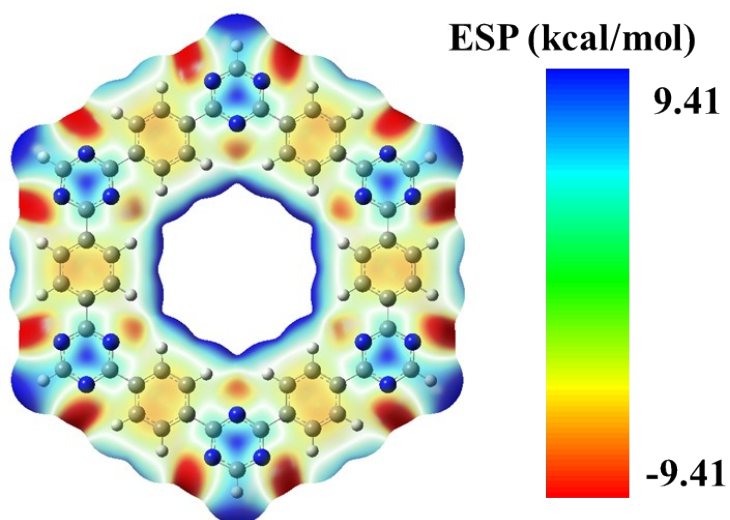


Figure S23. Molecular electrostatic potential (MESP) plots of CTF.

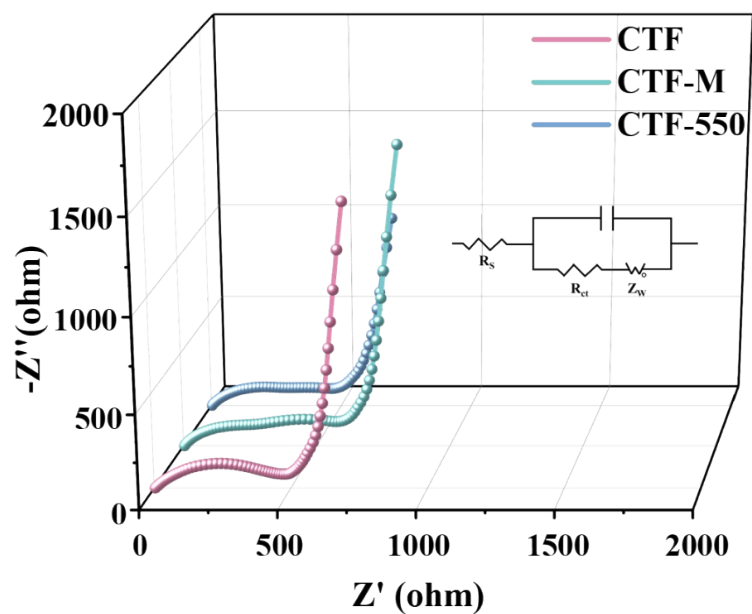


Figure S24. Nyquist plots of CTF, CTF-M, and CTF-550.

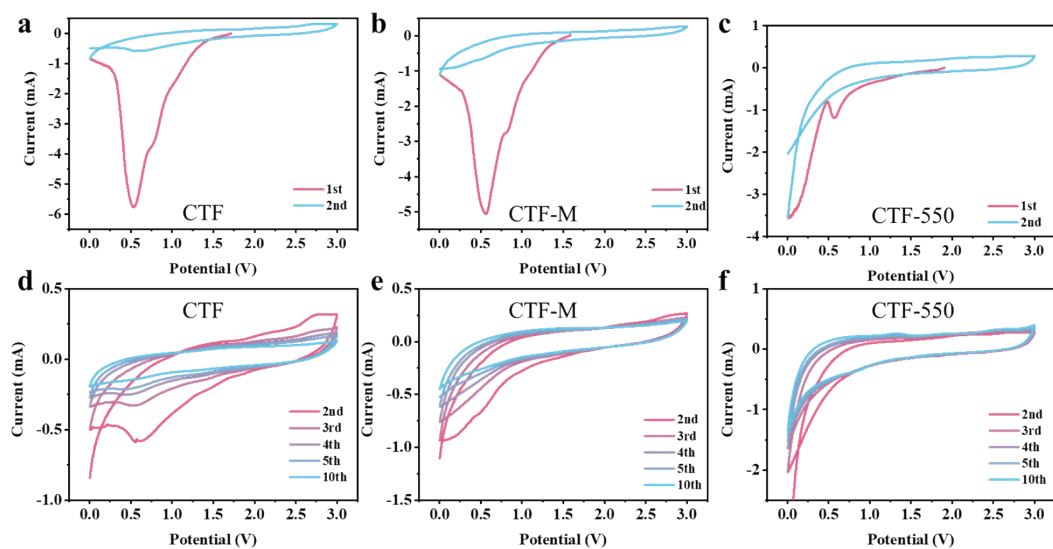


Figure S25. CV curves of (a, d) CTF, (b, e) CTF-M, and (c, f) CTF-550 at 5 mV s^{-1} .

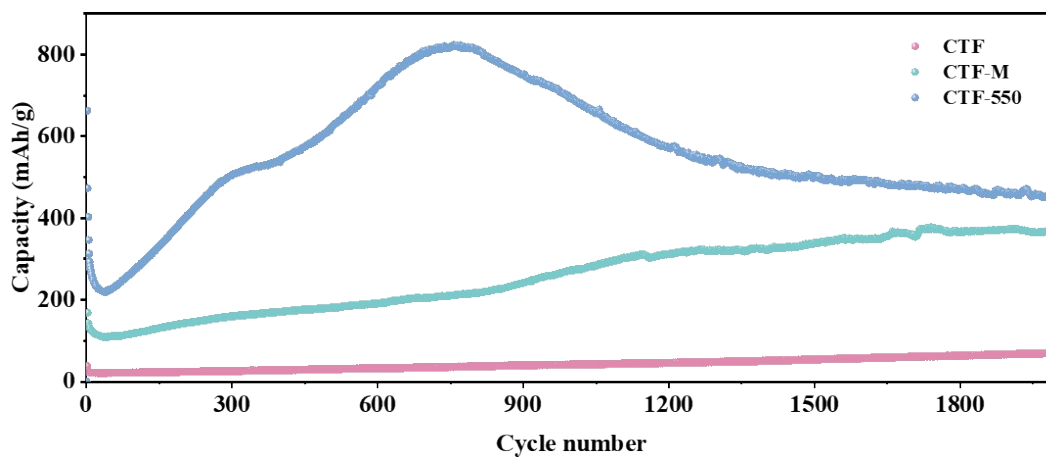


Figure S26. Long-term cycling stability of CTF, CTF-M, and CTF-550 at 1 A g^{-1} .

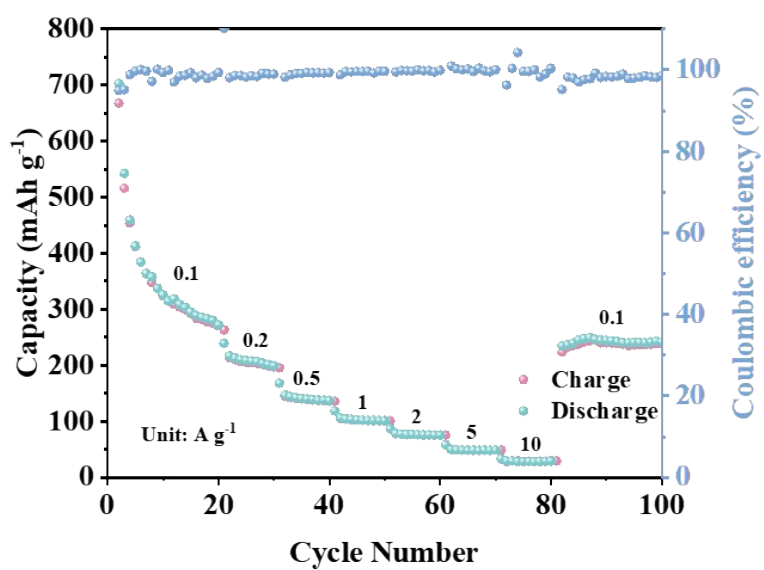


Figure S27. Rate performance of the CTF-AA as the anode.

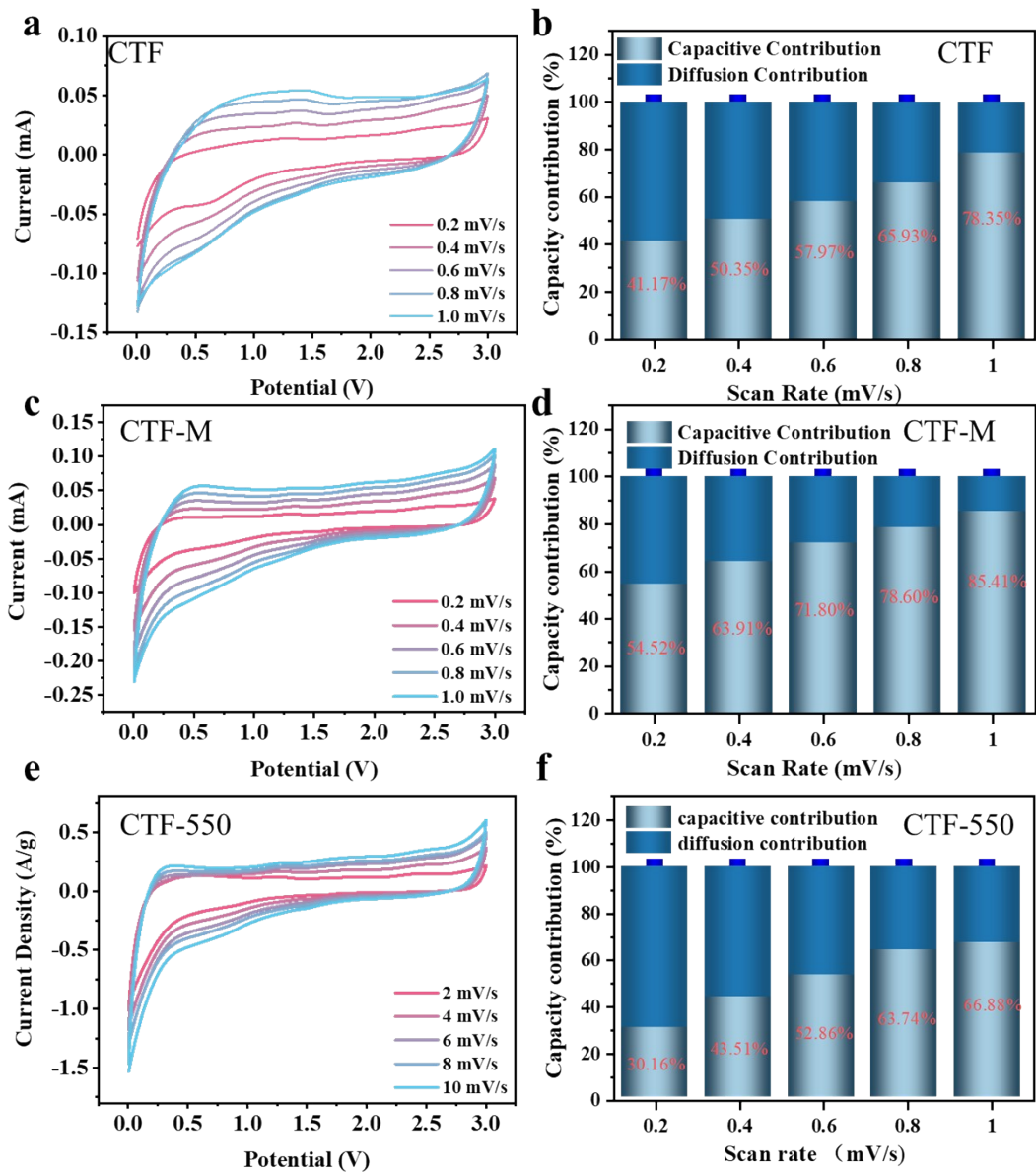


Figure S28. CV curves of (a) CTF, (c) CTF-M and (e) CTF-550 obtained at different scan rates. Contribution ratio of diffusion controlled and capacitive capacity of (b) CTF, (d) CTF-M and (f) CTF-550 at different scan rates.

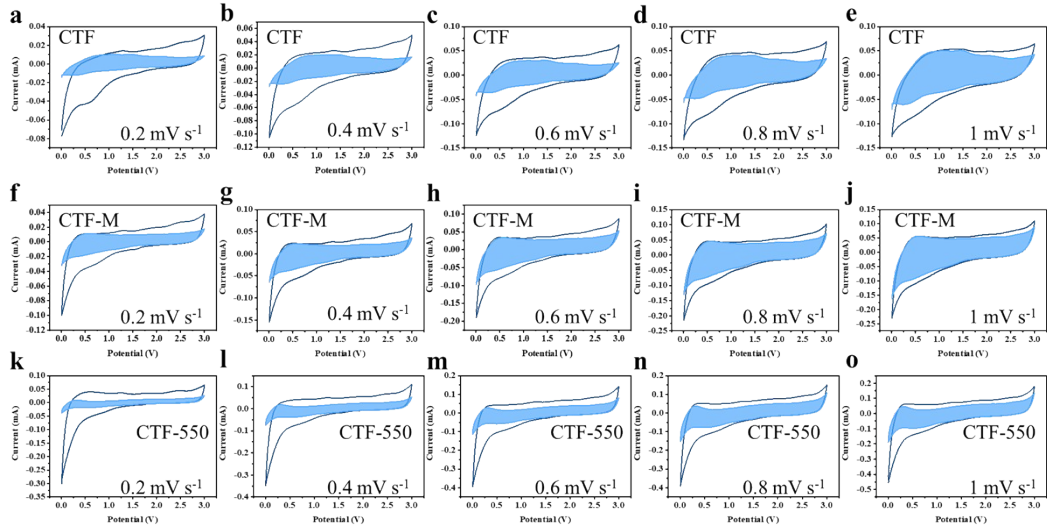


Figure S29. The calculated capacitive current-potential curves (blue regions) at different scan rates (0.2 mV s^{-1} ; 0.4 mV s^{-1} ; 0.6 mV s^{-1} ; 0.8 mV s^{-1} ; 1 mV s^{-1}). (a-e) CTF, (f-j) CTF-M, (k-o) CTF-550.

As is known, the current response can be divided into two parts: diffusion control contribution and capacitive contribution. The relationship between scan rate (v) and

current (i) can be expressed as follows: $i(V) = k_1v + k_2v^{\frac{1}{2}}$. Figure S27 showed the CV profiles of CTF-550, CTF and CTF-M at different scan rates from 0.2 mV s^{-1} to 1.0 mV s^{-1} , and the capacitance contributions at different scan rates were shown in Figure S29 (blue region). It was found that at the same scan rate, CTF-550 had the lowest percentage of capacitance contribution, and CTF-M had the highest one (Figure S28).

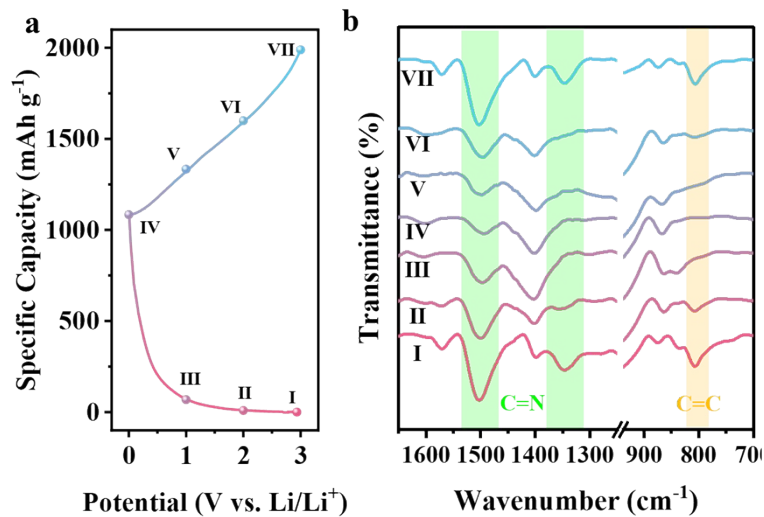


Figure S30. Ex situ FT-IR spectra of the CTF-550 electrode at different discharge and charge states, (a) charge/discharge curves. (b) FT-IR spectra.

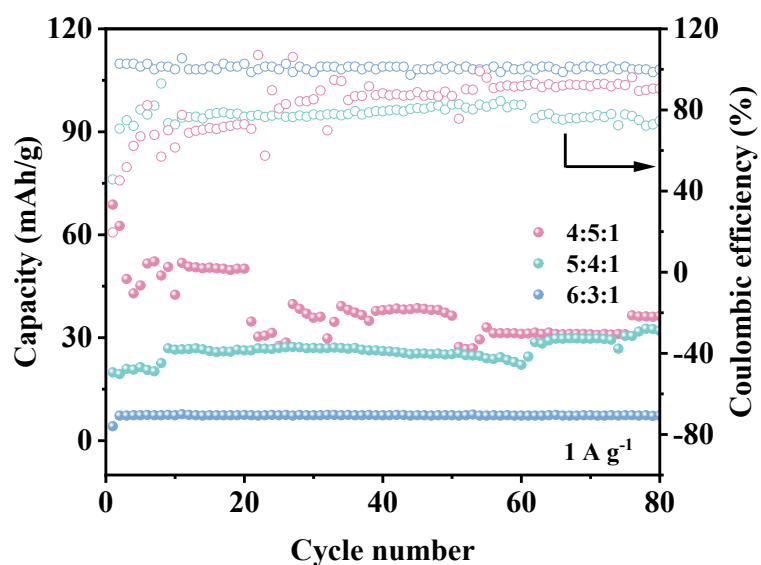


Figure S31. Cycling performance of CTF-M//CTF-550 full battery with the weight ratios of CTF-M, ketjen black and PVDF 6:3:1, 5:4:1 and 4:5:1 at 1 A g^{-1} .

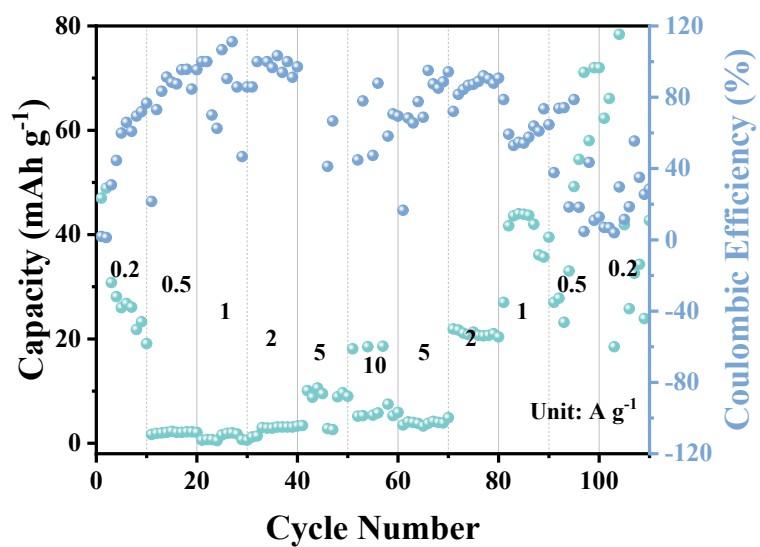


Figure S32. Rate performance of CTF-M//CTF-550 full battery with the weight ratios of CTF-M, ketjen black and PVDF 4:5:1.

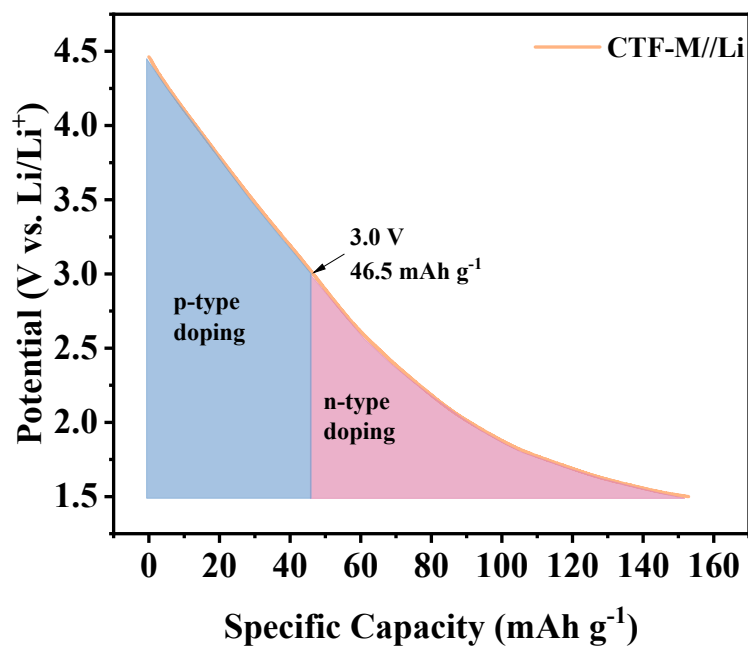


Figure S33. Discharge curve of CTF-M//Li with the weight ratio of CTF-M, ketjen black and PVDF 4:5:1 at 0.2 A g⁻¹, and its corresponding n-type and p-type doping capacity contributions.

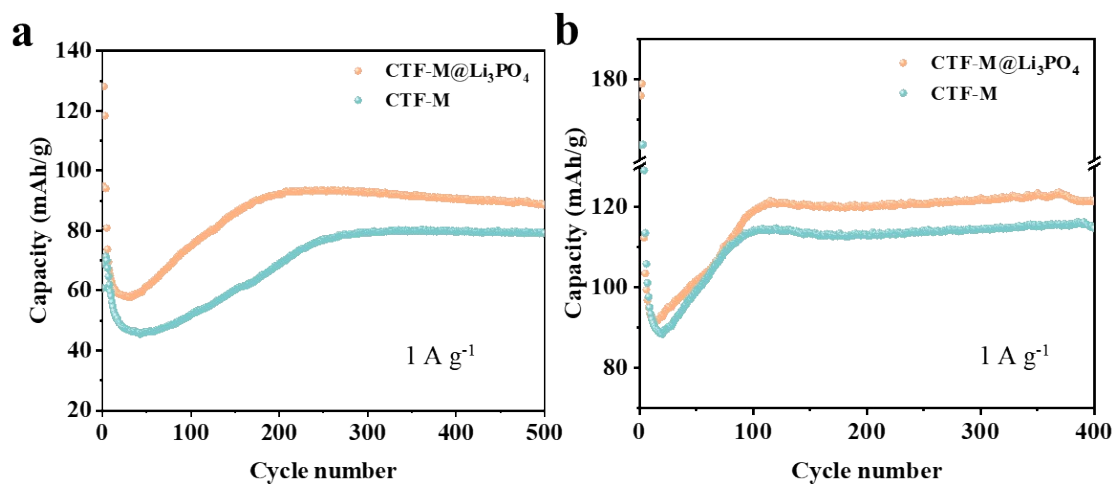


Figure S34. Cycling performance of CTF-M//Li and CTF-M@Li₃PO₄//Li with the weight ratios of CTF-M, ketjen black and PVDF (a) 5:4:1, (b) 4:5:1 at 1 A g⁻¹.

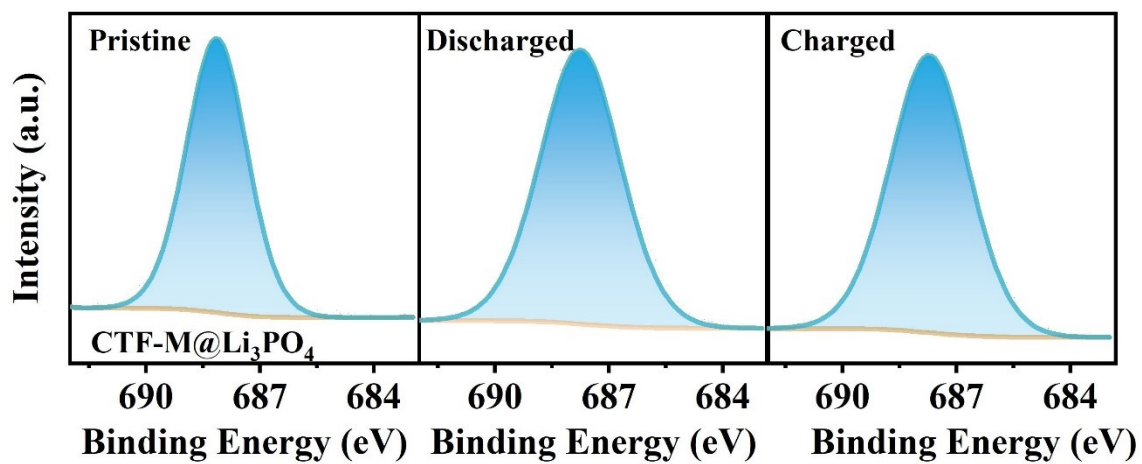


Figure S35. XPS spectra of F 1s of CTF-M@Li₃PO₄ at different charge/discharge states.

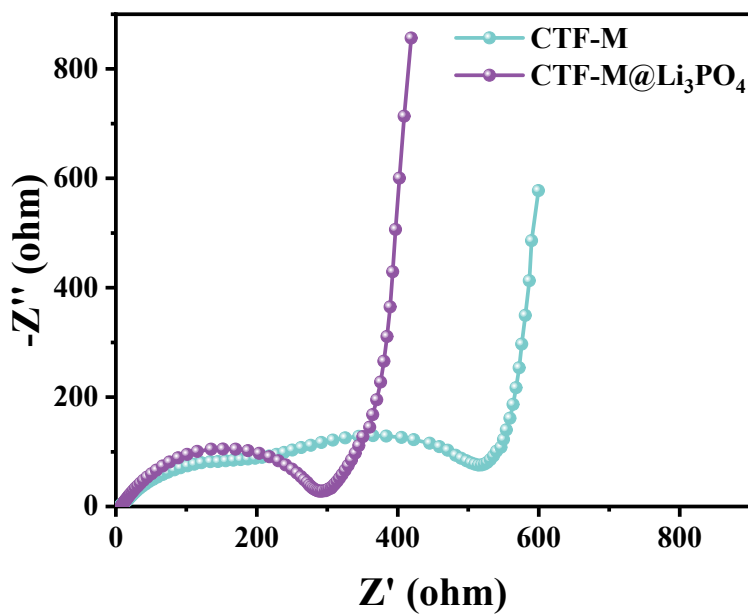


Figure S36. EIS of CTF-M and CTF-M-Li₃PO₄ with the weight ratios of CTF-M, ketjen black and PVDF 4:5:1.

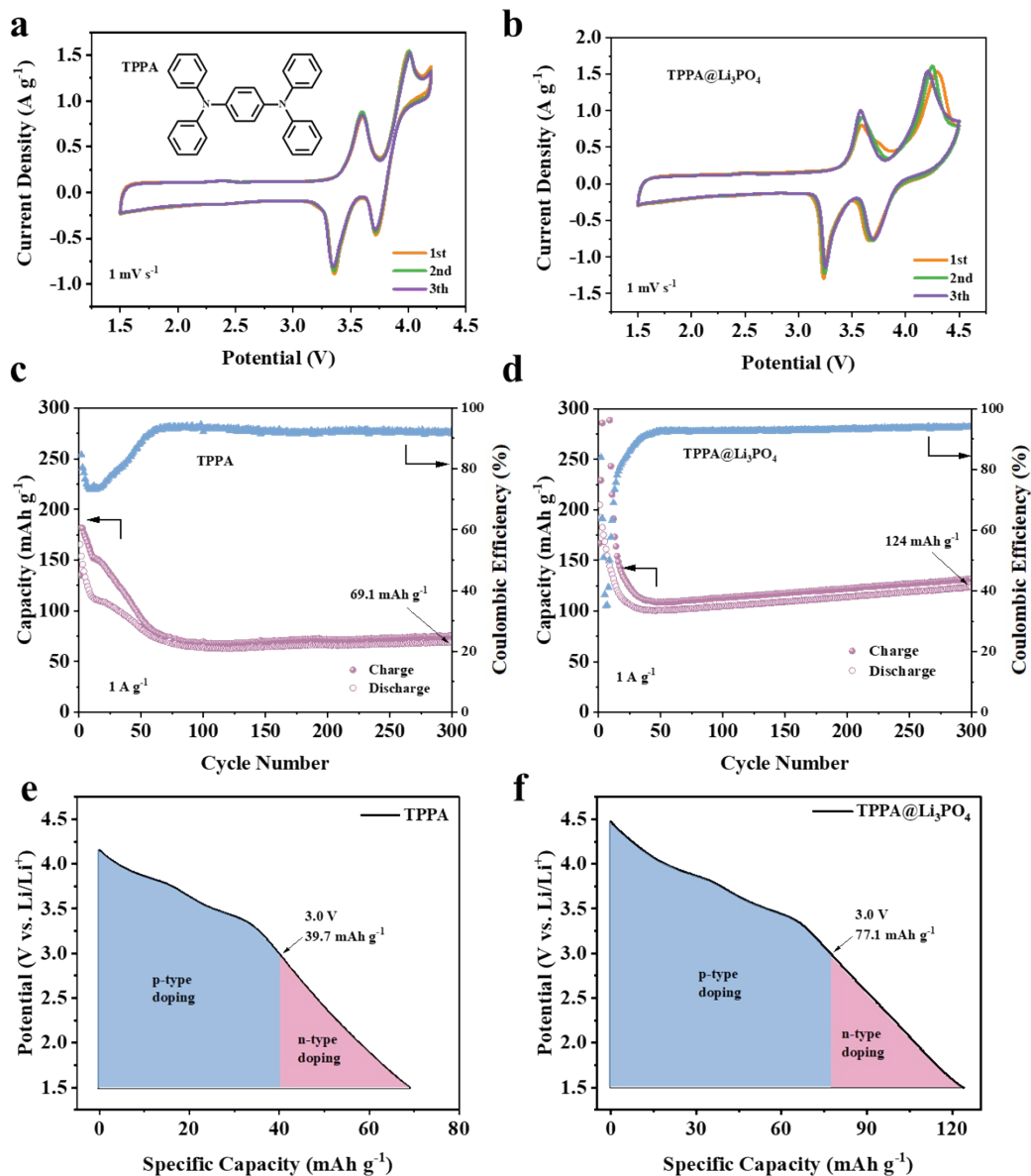


Figure S37. CV curves of (a) TPPA and (b) TPPA@Li₃PO₄ at 1 mV s⁻¹. Cycling performance of (c) TPPA and (d) TPPA@Li₃PO₄ at 1 A g⁻¹. Discharge curve of (e) TPPA and (f) TPPA @Li₃PO₄ at 1 A g⁻¹, and its corresponding n-type and p-type doping capacity contributions.

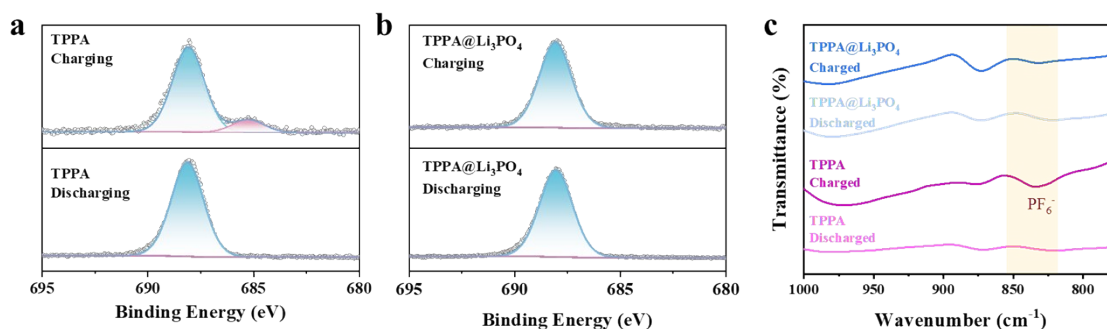


Figure S38. (a) XPS spectra of F 1s of TPPA at charge/discharge states. (b) XPS spectra of F 1s of TPPA@Li₃PO₄ at charge/discharge states. (c) FT-IR spectra of TPPA and TPPA@Li₃PO₄ at charge/discharge states.

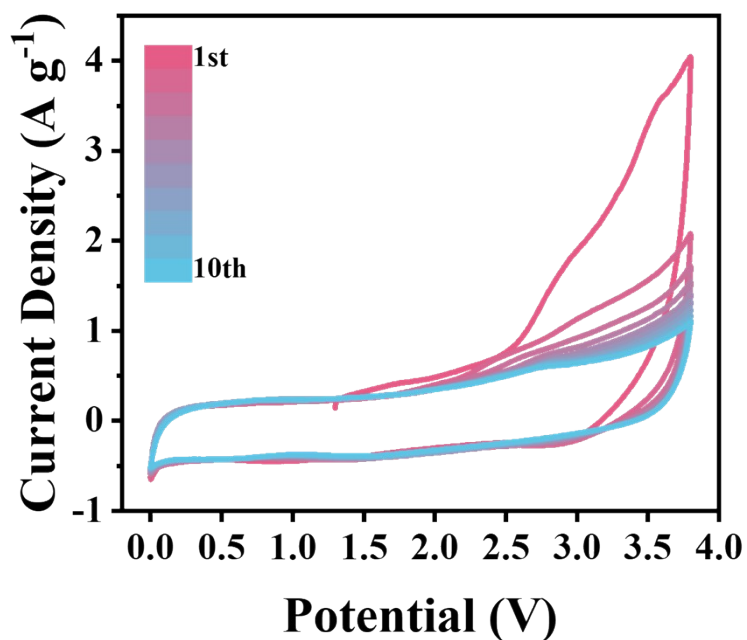


Figure S39. CV curves of CTF-M@Li₃PO₄//CTF-550 at 5 mV s⁻¹.

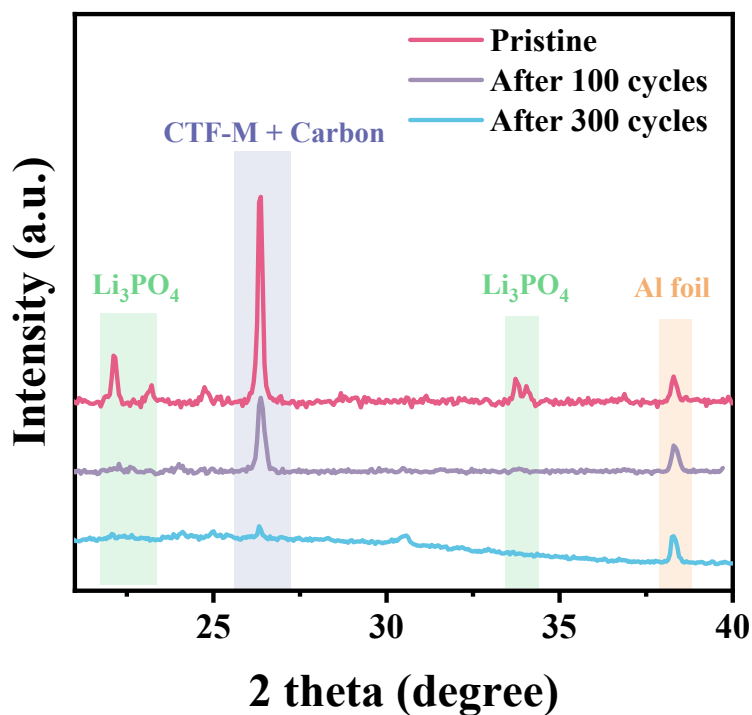
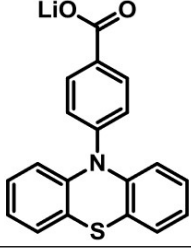
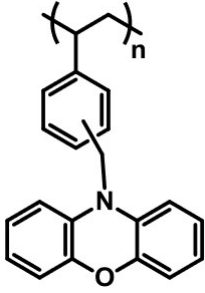
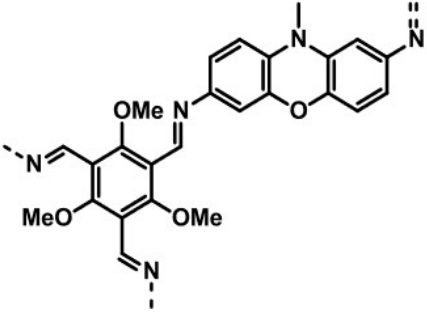
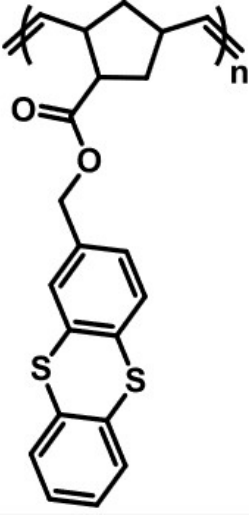
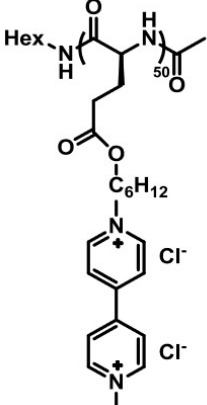

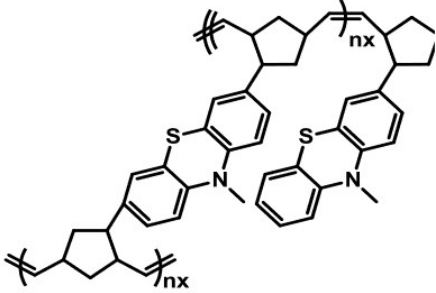
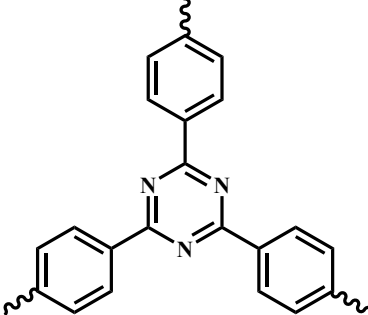


Figure S40. XRD spectra of the cathode of RCBs after different cycles.

Table S3. The comparison of the performance of p-type organic electrode materials in lithium-ion batteries.

Compound Name	Chemical Structure	Specific Capacity (mAh g ⁻¹)	Current density (A g ⁻¹)	Ref.
PDPPD		102	0.1	13
DCN		59.9	0.5	14
PVMPT		50	0.1	15
P1a		34.7	0.03	16

LiPHB		66	0.03	17
POEP		86.8	0.025	18
DAPO- TpOMe- COF		81.9	0.1	19
TT(P1)		66	0.07	20
viol-Cl		74.2	0.1	21

	 <p>The structure shows a polymer chain with a hexyl amide group (Hex-NH-CO-), a secondary amide group (NH-CO-), and a dicationic pyridinium salt chain (C₆H₁₂-N⁺-C₆H₄-N⁺-C₆H₄-Cl⁻-Cl⁻).</p>			
Coronene	 <p>Chemical structure of Coronene, a polycyclic aromatic hydrocarbon consisting of seven fused benzene rings.</p>	39.9	0.02	22
X-PNMPT	 <p>The structure shows a polymer chain with a central benzothiazole ring system and two side chains, one of which is labeled 'nx'.</p>	64	0.85	23
CTF-M@Li ₃ PO ₄ composite electrode	 <p>The structure shows a central benzothiazole ring system with two side chains, one of which is labeled 'nx'.</p>	101.2	0.2	This work

- 1 M. J. Abraham, T. Murtola, R. Schulz, S. Páll, J. C. Smith, B. Hess and E. Lindahl, *SoftwareX*, 2015, **1–2**, 19–25.
- 2 C. Lee, W. Yang and R. G. Parr, *Phys. Rev. B*, 1988, **37**, 785–789.
- 3 A. D. Becke, *The Journal of Chemical Physics*, 1993, **98**, 1372–1377.
- 4 S. Ren, M. J. Bojdys, R. Dawson, A. Laybourn, Y. Z. Khimyak, D. J. Adams and A. I. Cooper, *Advanced Materials*, 2012, **24**, 2357–2361.
- 5 M. Liu, Q. Huang, S. Wang, Z. Li, B. Li, S. Jin and B. Tan, *Angew. Chem.*, 2018, **130**, 12144–12148.
- 6 L. Guan, G. Cheng, B. Tan and S. Jin, *Chem. Commun.*, 2021, **57**, 5147–5150.
- 7 X. Zhu, C. Tian, S. M. Mahurin, S.-H. Chai, C. Wang, S. Brown, G. M. Veith, H. Luo, H. Liu and S. Dai, *J. Am. Chem. Soc.*, 2012, **134**, 10478–10484.
- 8 P. Kuhn, M. Antonietti and A. Thomas, *Angew. Chem. Int. Ed.*, 2008, **47**, 3450–3453.
- 9 Z. Lan, M. Wu, Z. Fang, Y. Zhang, X. Chen, G. Zhang and X. Wang, *Angew Chem Int Ed*, 2022, **61**, e202201482.
- 10 T. Zhou, Y. Zhao, J. W. Choi and A. Coskun, *Angewandte Chemie International Edition*, 2019, **58**, 16795–16799.
- 11 S.-Y. Yu, J. Mahmood, H.-J. Noh, J.-M. Seo, S.-M. Jung, S.-H. Shin, Y.-K. Im, I.-Y. Jeon and J.-B. Baek, *Angewandte Chemie International Edition*, 2018, **57**, 8438–8442.
- 12 T. Sun, Y. Liang, W. Luo, L. Zhang, X. Cao and Y. Xu, *Angewandte Chemie International Edition*, 2022, **61**, e202203327.
- 13 F. A. Obrezkov, A. F. Shestakov, V. F. Traven, K. J. Stevenson and P. A. Troshin, *J. Mater. Chem. A*, 2019, **7**, 11430–11437.
- 14 Z. Wang, J. Yang, Z. Chen, L. Ye and Y. Xu, *ChemSusChem*, 2021, **14**, 4573–4582.
- 15 M. Kolek, F. Otteny, P. Schmidt, C. Mück-Lichtenfeld, C. Einholz, J. Becking, E. Schleicher, M. Winter, P. Bieker and B. Esser, *Energy Environ. Sci.*, 2017, **10**, 2334–2341.
- 16 P. Acker, L. Rzesny, C. F. N. Marchiori, C. M. Araujo and B. Esser, *Advanced Functional Materials*, 2019, **29**, 1906436.

- 17M. Rajesh, F. Dolhem, C. Davoisne and M. Becuwe, *ChemSusChem*, 2020, **13**, 2364–2370.
- 18X. Zhang, Q. Xu, S. Wang, Y. Tang and X. Huang, *ACS Appl. Energy Mater.*, 2021, **4**, 11787–11792.
- 19Z. Meng, Y. Zhang, M. Dong, Y. Zhang, F. Cui, T.-P. Loh, Y. Jin, W. Zhang, H. Yang and Y. Du, *J. Mater. Chem. A*, 2021, **9**, 10661–10665.
- 20M. E. Speer, M. Kolek, J. J. Jassoy, J. Heine, M. Winter, P. M. Bieker and B. Esser, *Chem. Commun.*, 2015, **51**, 15261–15264.
- 21T. P. Nguyen, A. D. Easley, N. Kang, S. Khan, S.-M. Lim, Y. H. Rezenom, S. Wang, D. K. Tran, J. Fan, R. A. Letteri, X. He, L. Su, C.-H. Yu, J. L. Lutkenhaus and K. L. Wooley, *Nature*, 2021, **593**, 61–66.
- 22I. A. Rodríguez-Pérez, Z. Jian, P. K. Waldenmaier, J. W. Palmisano, R. S. Chandrabose, X. Wang, M. M. Lerner, R. G. Carter and X. Ji, *ACS Energy Lett.*, 2016, **1**, 719–723.
- 23F. Otteny, G. Studer, M. Kolek, P. Bieker, M. Winter and B. Esser, *ChemSusChem*, 2020, **13**, 2232–2238.